Available online at www.sciencedirect.com
SCIENCE DIRECT®
Composite Structures 66 (2004) 317–326
COMPOSITE STRUCTURES
www.elsevier.com/locate/compstruct

Determination of dynamic strain profile and delamination detection of composite structures using embedded multiplexed fibre-optic sensors

Hang-Yin Ling, Kin-Tak Lau *, Li Cheng

Department of Mechanical Engineering, The Hong Kong Polytechnic University, Hung Hom, Kowloon, Hong Kong, China

Available online 17 June 2004

Abstract

This paper studies the dynamic strain measurement and delamination detection of clamped–clamped composite structures using embedded multiplexed Fibre-optic Bragg grating (FBG) sensors through experimental and theoretical approaches. A dynamic strain calibration of the FBG sensors and surface mounted strain gauges to find out the correlation between the strain and photovoltage is reported. The embedded FBG sensors were used to measure the natural frequency and dynamic strain of intact and delaminated composite structures. The strain profile of these structures subjected to external excitations was evaluated by using experimental measured data and a modified vibration theory. The results revealed that the use of the embedded FBG sensors is able to actually measure the dynamic strain and identify the existence of delamination of the structures. This allows the continuous estimation of fatigue life and minimises the need of in-site inspection of the structures.

Keywords: Fibre-optic sensors; Structural health monitoring; Dynamic measurement

1. Introduction

With the rapid aging of civil infrastructures and of both military and commercial aircrafts, a significant research attention has been directed over the recent years towards the field of structural health monitoring. Novel methodologies in detecting and monitoring structural degradation are necessary to extend the service life and to minimise the time and cost for maintenance of current structures. Advanced composite materials have been widely used in a variety of load-bearing structures such as rotor blades, aircraft's fuselage and wing structures because of their good specific stiffness and strength as well as excellent corrosion resistance in the past decade. These structures are always subjected to unexpected external excitations at various vibration frequency ranges. These dynamic interferences may cause the structures suffering from fatigue damages and/or catastrophic failures due to an excitation frequency approaches to the natural frequencies of the structures. Therefore, vibration monitoring and damage detection are the two main concerns in the area of structural health monitoring of composite structures.

Fibre-optic Bragg grating (FBG) sensors are widely accepted as embedded strain and vibration monitoring devices for advanced composite structures [1]. The advantages of using the FBG sensors include their small physical size, insensitivity to electromagnetic interference, lightweight, multiplexability and ability to be used at relatively high temperature and environmentally unfavourable conditions. However, most research related to the use of embedded FBG sensors has only focused on the static strain measurement [2] and identification of vibration mode shapes of the structures [3]. Under dynamically operating conditions, Read and Foote [4] experimentally demonstrated the feasibility of using a FBG sensor system in real-time structural health monitoring of sea and flight trials. Kim et al. [5] also measured dynamic strains inside a subscale wing structure under real-time wind tunnel testing by using FBG sensors. However, only little attentions provide comprehensive study on dynamic strain measurements that truly respond to the mechanical performance of structures, on using the embedded FBG sensors.

* Corresponding author. Tel.: +852-2766-7730; fax: +852-2365-4703.
E-mail address: mmktlau@polyu.edu.hk (K.-T. Lau).

0263-8223/$ - see front matter © 2004 Elsevier Ltd. All rights reserved.
doi:10.1016/j.compstruct.2004.04.054

Since the mechanical properties of composite materials may degrade severely in the presence of damage, the damage detection is an important issue to maintain the structural integrity. Delamination, debonding of adjoining cracks in matrix materials, separation of adjoining piles, and broken fibres originated during manufacturing are the most severe damages occur in advanced composite structures. Delamination is the most destructive type of damage among others since this damage cannot be visibly detected. Composite laminates can usually be modelled as four separated beam segments to investigate the effects of delamination [6]. An early model developed by Wang et al. [7] assumed that two delaminated segments can be independently displaced, but it resulted in a physically impossible interpenetration of the delaminated segments. Mujumdar and Suryanarayan [8] developed a constrained mode model in which delaminated segments are constrained to have identical transverse displacement. As it is a simple and more realistic model to arrive at a physical understanding of the basic effect of the delamination in order to provide the general information for delamination detection, this mathematical model would be employed in this project.

In this paper, the feasibility of using embedded multiplexed FBG sensors as dynamic strain and vibration monitoring devices for intact and delaminated composite beams under various external excitations is presented. The principle of dynamic strain measurements with the FBG sensors is also discussed. The effect of delamination on the dynamic strain profile and natural frequency of a composite beam is theoretically investigated. A comparison of the results extracted from a FBG sensor, a laser vibrometer and an accelerometer is given. The potentiality of using an embedded multiplexed FBG sensor system for delamination detection is also discussed.

2. Strain sensing principle of FBG sensors

The principle of FBG strain sensor is to measure the change of reflected signal from a grating when it is subjected to elongation. This change would influence the reflective index (n_b) and spatial pitch Λ at the core section of the sensor [9]. A schematic illustration of the FBG system for strain measurement is shown in Fig. 1.

To utilise the FBG sensor for the strain measurement, a grating, which acts essentially as a wavelength selective mirror, must be firstly written in the core of an optical fibre as demonstrated in Fig. 1. The grating is written by exposing the fibre to a pair of strong Ultra-violet (UV) interference signal. This method of grating writing for strain and temperature measurements is called "Phase mask technique". According to the Bragg law, the Bragg

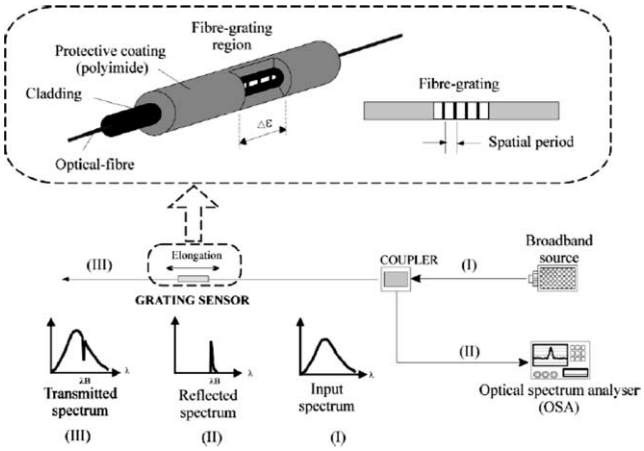

Fig. 1. FBG strain measuring system.

wavelength (λ_B) that is reflected from the sensor is given by

$$\lambda_B = 2n_b\Lambda \tag{1}$$

Any changes of strain in the grating region result in changing of spatial period and core refractive index. The measurement of the mechanical strain (ε_g) is determined by the variation of the Bragg wavelength shift ($\Delta\lambda_B$) [10]. By neglecting the temperature effect of the sensor and the strain transfer to the fibre in transverse direction, the change of the Bragg wavelength can be expressed as

$$\Delta\lambda_B = K\varepsilon_g \tag{2}$$

where K is called "Theoretical gauge constant" [11], which can be determined experimentally.

3. Dynamic calibrations of FBG sensors

Calibration of FBG sensors should be conducted separately for static and dynamic strain measurements. In the static case, a gauge constant is generally obtained by the relationship between the measured change of strain and the corresponding reflective wavelength shift [2]. For measuring dynamic strains, a conversion factor of FBG strain measuring system is determined to relate the strain changes and photovoltage variation.

Owing to the dependence of the photodetector output denoted by photovoltage-variation (ΔV_{photo}) and the wavelength shift ($\Delta\lambda_B$) when the signal passes through the OTF Transmitted Spectrum, the linear relationship between the photovoltage (ΔV_{photo}) and the wavelength shift ($\Delta\lambda_B$) is obtained. This relationship can be expressed as

$$\Delta V_{photo} = C\Delta\lambda_B \tag{3}$$

where C is the proportional constant which depends on a desirable system. By combining Eqs. (2) and (3), a following equation is formed:

$$\Delta V_{\text{photo}} = S\,\Delta\varepsilon_{\text{g}} \tag{4}$$

where $S = C \cdot K$. It is reminded that the photodetector output is related to the power of the SLED and the power loss such as the reflectivity of grating, splice loss of fibre, insertion loss of TOF and the power splitting reduction through the coupler, of the above FBG measurement set up. A signal analyser was used in this experiment to detect the photovoltage output.

A dynamic calibration test of a clamped–clamped glass-fibre composite beam with an embedded FBG sensor, subjected to an out-of-plate vibration motion at different frequency ranges, was conducted. Ten layers of 0°/90° E-glass fabric and Epoxy-based resin (Araldite MY 750) were used to fabricate the beam. A single optical fibre with pre-written grating sensor was embedded between the 9th and 10th layers for which measuring from the top surface of the beam during the lay up process. Fig. 2 shows an experiment setup of the beam with the embedded FBG sensor and a surface bonded strain gauge on its corresponding surface. The beam was clamped rigidly at both ends. An electric-driven shaker was attached to the bottom surface of the beam at a position 100 mm from the left end and to generate external excitations to the beam. A force transducer was placed between the shaker's stinger and the beam. The photovoltage and strain measured by the embedded sensor and the strain gauge were recorded simultaneously.

In Fig. 3, the dynamic responses measured from the strain gauge and the FBG sensor are plotted. It is obvious that both the strain sensing devices were able to indicate the first natural frequency of the beam, $f_1 = 80$ Hz. However, there were some deviations of the measurements when the vibration frequency exceeded 100 Hz. The second natural frequency's peak shown by the FBG sensor is much more obvious that than of the strain gauge. A small plateau is shown on the lower curve, and thus the second natural frequency of the beam is hard to be identified by the strain gauge.

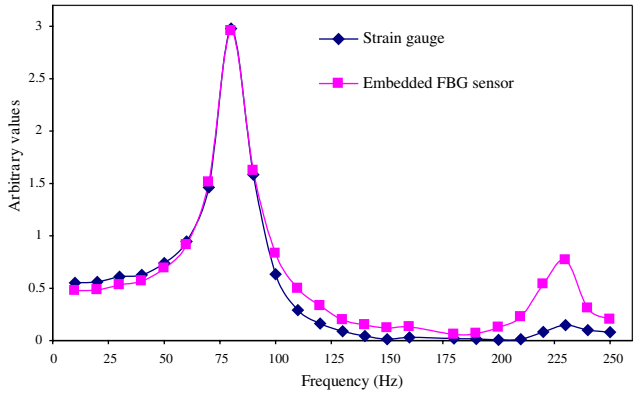

Fig. 3. Dynamic responses measured by the FBG sensor and strain gauge at applied frequencies below 250 Hz.

It is understandable that for the clamped–clamped beam, increasing the vibration frequency results in decreasing out-of-plane vibration amplitude, thus reducing the beam's surface strain. By using the strain gauge, it was found that inconsistent strain data were measured at strain values below 3 με. However, the photovoltage measured from the FBG sensors was more reliable. In Fig. 3, it is clearly revealed that the second natural frequency of the beam, $f_2 = 230$ Hz, is sharply shown by the peak of the upper curve and this value satisfies with the results addressed by Clarence [12].

Based on these results, the constant value S as indicated in Eq. (4) was determined as 0.5898 using the measured data shown in Fig. 3 at the frequency regions between 25 and 100 Hz, and between 220 and 240 Hz. The relationship between normalised vibration amplitude, strains measured by the strain gauge and evaluated by Eq. (4) is plotted in Fig. 4. In the figure, it is found that no strains were measured by the strain gauge at the normalised vibration amplitude below 0.0011, while the FBG sensor still provides actual strain data within this region. The scatter in results for normalised vibration amplitudes between 0.0004 and 0.0008 might be due to

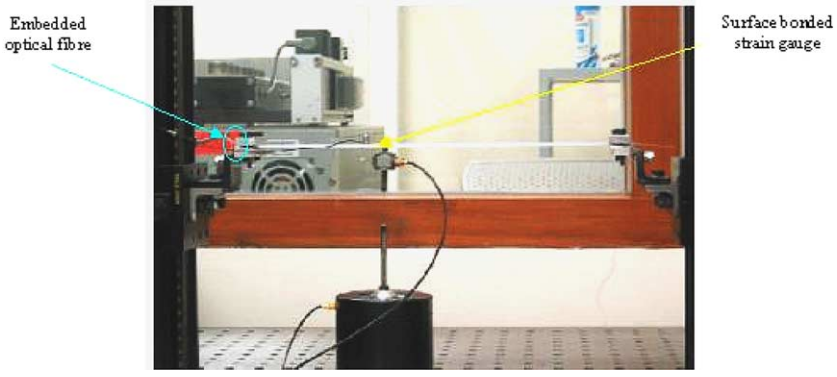

Fig. 2. Dependence of photovoltage and wavelength shift.

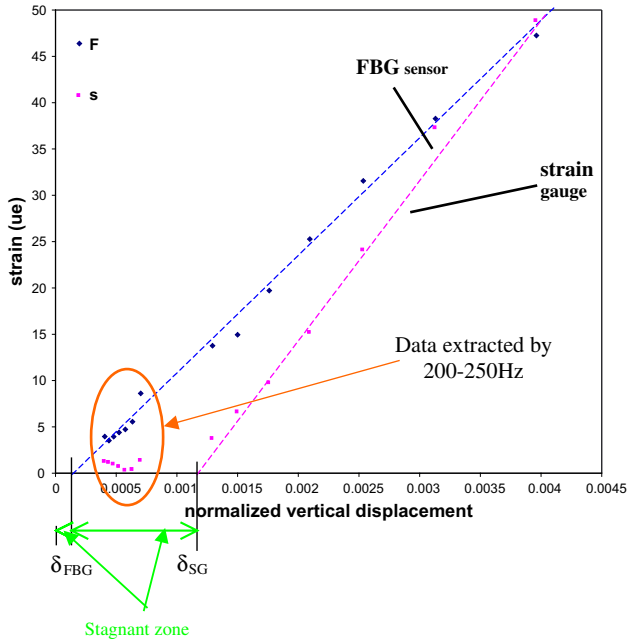

Fig. 4. Plot of the strain against normalised vertical displacement of the strains measured by the strain gauge and FBG sensor.

the low sensitivity of the strain gauge for strains below 3 με.

4. Determination of dynamic strain profile of a composite beam using embedded multiplied FBG sensors

As the strain distribution along the beam is of interest, theoretical strain mode shapes of different vibration modes have to be studied. To obtain the strain mode shapes of the beam, the relationship between strain and lateral deflection of the beam is examined. The relationship between the strain and lateral deflection of the beam can be expressed as [12]

$$\varepsilon(x) = y\frac{\partial^2 w(x)}{\partial x^2} \tag{5}$$

From Eq. (5), it is known that the strain of the beam is proportional to the second derivative of that lateral displacement. For the clamped–clamped beam, the displacement mode shape at the mode i can be expressed as

$$\phi_i(x) = \sin\lambda_i x - \sinh\lambda_i x + \alpha_i[-\cos\lambda_i x + \cosh\lambda_i x] \tag{6}$$

where

$$\alpha_i = \frac{\sinh\lambda_i L - \sin\lambda_i L}{\cosh\lambda_i L - \cos\lambda_i L}$$

for first three modes, $\lambda_i L = 4.73$, 7.85 and 10.99 ($i = 1$, 2 and 3); A_i is the vibration amplitude at mode i, which depends on the excitation force; w_i is the lateral displacement at mode i. And

$$w(x) = \sum_{i=1}^{n} A_i\phi_i(x). \tag{7}$$

Since the structural response is dominated by the mode i at ith natural frequency, by considering the structural resonance cases only, the lateral displacement can be simply expressed by

$$w_i(x) = A_i\phi_i(x) \tag{8}$$

Therefore, the strain mode shape is

$$\begin{aligned}\varepsilon(x) &= y\frac{\partial^2 w(x)}{\partial x^2}\\ &= K_i\{-\sin\lambda_i x - \sinh\lambda_i x + \alpha_i(\cos\lambda_i x + \cosh\lambda_i x)\}\end{aligned} \tag{9}$$

where $K_i = yA_i\lambda_i^2$ is a constant at mode i.

The strain mode shapes of the clamped–clamped beam for the first three modes are plotted in Fig. 5. The amplitude of strain mode shape decreases with increasing of the mode number.

In certain vibrating modes, the ratio of strain measured at two different points along the beam is constant. To ensure the uniqueness of this ratio, the locations where the sensors are installed, must not be symmetric of the beam's centre. For two given points along the beam, denoted by X_1 and X_2, the theoretical strain values at mode i are

$$\varepsilon_i(x_1) = y\frac{\partial^2 w_i(x_1)}{\partial x^2} \tag{10}$$

$$\varepsilon_i(x_2) = y\frac{\partial^2 w_i(x_2)}{\partial x^2} \tag{11}$$

The strain ratio is given by

$$\frac{\varepsilon_i(x_1)}{\varepsilon_i(x_2)} = \frac{w_i''(x_1)}{w_i''(x_2)} = \frac{\phi_i''(x_1)}{\phi_i''(x_2)} \tag{12}$$

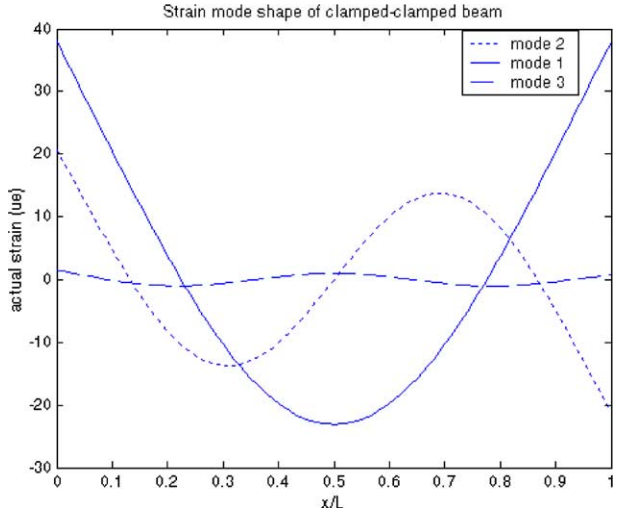

Fig. 5. Strain mode shapes of a clamped–clamped composite beam for first three modes.

To evaluate the strain profiles of a clamped–clamped composite beam, two multiplexed FBG sensors were embedded into the beam. The conversion factors (S's) between the strains extracted by strain gauges and photovoltages of the FBG sensors was calculated using the experimental measuring results. The conversion factors (S) for the 1st and 2nd sensors were 0.6159 and 0.5765 respectively. A voltage input range was from 100 to 450 mV, a total of eight voltage inputs were used to excite the composite beam. The photovoltages are recorded by the FBG sensors at points, X_1 and X_2 by Eq. (4), the relationship between the strains is

$$\frac{V_{\mathrm{FBG}_i}(x_1)}{V_{\mathrm{FBG}_i}(x_2)} = \frac{S_1 \varepsilon_{\mathrm{measured}_i}(x_1)}{S_2 \varepsilon_{\mathrm{measured}_i}(x_2)}$$
$$\Rightarrow \quad \frac{\varepsilon_{\mathrm{measured}_i}(x_1)}{\varepsilon_{\mathrm{measured}_i}(x_2)} = \frac{S_2 V_{\mathrm{FBG}_i}(x_1)}{S_1 V_{\mathrm{FBG}_i}(x_2)} \tag{13}$$

Table 1 lists the experimental and theoretical surface strain ratios at the first three vibration modes. It is found that the measured strain ratio extracted from the FBG sensors was close to the theoretical one. Therefore, it is reasonable to conclude that the use of FBG sensors is able to evaluate the strain profile along the beam at the first three vibrating modes. Referring to Eq. (9), the constant K_i can be calculated once the strain of the beam is known.

5. Constrained beam model

Fig. 6 shows a constrained beam model with an arbitrarily located through-width delamination developed by Mujumdar and Suryanarayan in 1988 [8]. In this model, the beam is assumed to be homogenous and isotropic. For the sake of simplicity, only a single delamination is considered. Also, it is assumed that there is no gap between the layers at the delamination region under all conditions such that this model was called the constrained model.

The governing equations for the transverse equilibrium for integral segments can be written in a dimensionless form as

$$\frac{\partial^4 \bar{w}_i}{\partial \bar{x}_i^4} + \left(\frac{\rho A L^4}{EI}\right) \frac{\partial^2 \bar{w}_i}{\partial t^2} = 0, \quad i = 1, 4 \tag{14}$$

where $\bar{w}_i = w_i/L$ and $\bar{u}_i = u_i/d$ are the dimensionless axial coordinate and the transverse displacement of the ith segment respectively.

For the delaminated segments, the governing equations can be written as

$$-EI_2 \frac{\partial^4 \bar{w}_2}{\partial \bar{x}_2^4} - P_d \frac{\partial^2 \bar{w}_2}{\partial \bar{x}_2^2} - \rho A_2 \frac{\partial^2 \bar{w}_2}{\partial t^2} - p = 0, \quad \text{for segment 2} \tag{15}$$

Table 1
Physical and mechanical properties of the beam

Vibration mode	Theoretical strain ratio	Measured strain ratio	Error between measured and theoretical values (%)
Mode 1	2.2936	2.3225	1.26
Mode 2	1.1158	1.0533	5.6
Mode 3	1.0829	1.1366	4.95

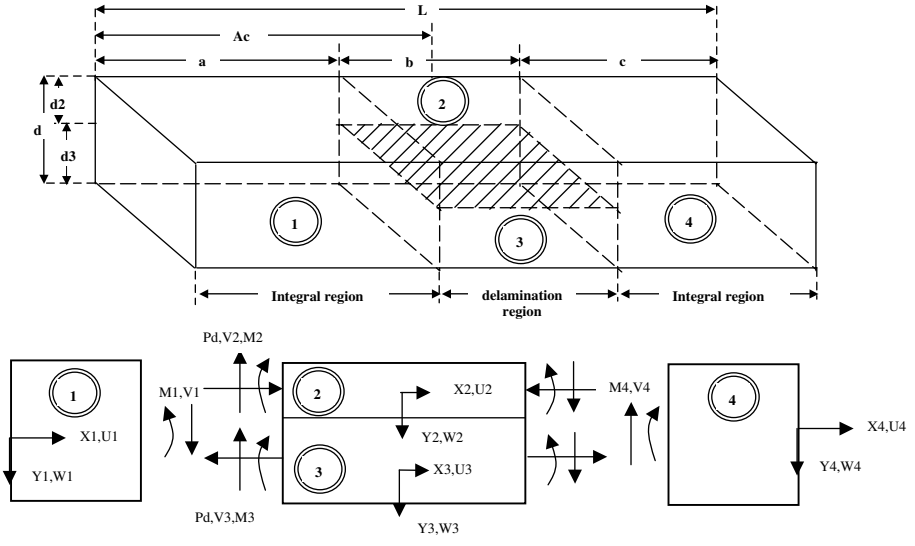

Fig. 6. Geometry and co-ordinate system of a constrained beam model [8].

$$-EI_3\frac{\partial^4\bar{w}_3}{\partial\bar{x}_3^4}+P_d\frac{\partial^2\bar{w}_3}{\partial\bar{x}_3^2}-\rho A_3\frac{\partial^2\bar{w}_3}{\partial t^2}+p=0,\quad \text{for segment 3} \tag{16}$$

where p is the normal contact pressure distribution between the two segments and P_d is the magnitude of an axial load in each segment.

As the axial load P_d depends on the amplitude and mode of deformation, the second terms on the left hand side in Eqs. (15) and (16) are nonlinear. Based on the free mode of deformation assumption, the nonlinear terms are not taken into account. Also, in the constrained model, w_2 is assumed to be equal to w_3 in everywhere in the delamination region and x_2 is equal to x_3. As the results, Eqs. (15) and (16) can be combined to represent the behaviour of the delaminated region and the equation in dimensionless form can be expressed as

$$\frac{\partial^4\bar{w}_2}{\partial\bar{x}_2^4}+\left(\frac{\rho(A_2+A_3)L^4}{E(I_2+I_3)}\right)\frac{\partial^2\bar{w}_2}{\partial t^2}=0 \tag{17}$$

The general solutions of Eqs. (14) and (17) can be written in the following form:

$$\bar{w}_i(\bar{x}_i)=F_iC_i \tag{18}$$

where

$$F_i=[f_{1i}(\bar{x}_i)\quad f_{2i}(\bar{x}_i)\quad f_{3i}(\bar{x}_i)\quad f_{4i}(\bar{x}_i)]$$
$$C_i=[c_{1i}\quad c_{2i}\quad c_{3i}\quad c_{4i}]^{\mathrm{T}}$$

in which

$$f_{1i}(x_i)=\sin(\lambda_i\bar{x}_i),\quad f_{2i}(x_i)=\cos(\lambda_i\bar{x}_i)$$
$$f_{3i}(x_i)=\sinh(\lambda_i\bar{x}_i),\quad f_{4i}(x_i)=\cosh(\lambda_i\bar{x}_i)$$

where the dimensionless frequency parameters, λ_i, are given by

$$\lambda_1^4=\lambda_4^4=\lambda^4=\rho A\omega^2L^4/EI$$
$$\lambda_2^4=\rho(A_2+A_3)\omega^2L^4/E(I_2+I_3)=\lambda^4/(\bar{d}_2^{\,3}+\bar{d}_3^{\,3})$$

in which $\bar{d}_2=d_2/d$ and $\bar{d}_3=d_3/d$.

By combining Eqs. (5) and (18), the strain along the whole beam can be expressed as

$$\bar{\varepsilon}(\bar{x})=\begin{cases}D_1C_1\in[0,\bar{a})\\ D_2C_2\in(-\bar{b},\bar{b})\\ D_3C_3\in(\bar{c},0]\end{cases} \tag{19}$$

where $D_i=[f_{1i,xx}(\bar{x}_i)\ \ f_{2i,xx}(\bar{x}_i)\ \ f_{3i,xx}(\bar{x}_i)\ \ f_{4i,xx}(\bar{x}_i)]$, in which $(\ )_{,xx}$ denotes the second derivative with respect to x_i. $\bar{a}=a/L$, $\bar{b}=b/L$ and $\bar{c}=c/L$ are the dimensionless length of the beam segments 1, 2 and 4 respectively.

6. Boundary and continuity conditions of a constrained beam model

For a clamped–clamped beam, the boundary conditions at $\bar{x}_1=\bar{x}_4=0$ are

$$\bar{w}_i=0\quad\text{and}\quad\partial\bar{w}_i/\partial\bar{x}_i=0\qquad\text{for } i=1 \text{ and } 4 \tag{20}$$

At the junction among beam segment 1, delaminated segments 2 and 3 represented by $\bar{x}_1=\bar{a}$ and $\bar{x}_2=-\bar{b}/2$ respectively and the continuity conditions are

continuity of transverse displacement:

$$\bar{w}_1=\bar{w}_2 \tag{21}$$

continuity of normal slopes:

$$\partial\bar{w}_1/\partial\bar{x}_1=\partial\bar{w}_2/\partial\bar{x}_2 \tag{22}$$

continuity of shear forces:

$$\partial^3\bar{w}_1/\partial\bar{x}_1^3=(\bar{d}_2^{\,3}+\bar{d}_3^{\,3})\partial^3\bar{w}_2/\partial\bar{x}_2^3 \tag{23}$$

continuity of bending moments:

$$\partial^2\bar{w}_1/\partial\bar{x}_1^2=(\bar{d}_2^{\,3}+\bar{d}_3^{\,3})\partial^2\bar{w}_2/\partial\bar{x}_2^2-P_dL^2/2EI \tag{24}$$

where the term P_dL^2/EI can be determined by the continuity of axial displacement of the beam segments, therefore,

$$P_dL^2/EI=(6\bar{d}_2\bar{d}_3/\bar{b})[\partial\bar{w}_1(\bar{a})/\partial\bar{z}_1-\partial\bar{w}_4(-\bar{c})/\partial\bar{z}_4].$$

Similarly, the continuity conditions at junction among beam segment 4, delaminated segments 2 and 3 represented by $\bar{x}_4=\bar{c}$ and $\bar{x}_2=\bar{b}/2$ are obtained by replacing $\bar{w}_1$ and $\bar{x}_1$ by $\bar{w}_4$ and $\bar{x}_4$ respectively in Eqs. (21)–(24). There is a set of 12 simultaneous linear homogenous algebraic equations in 12 unknown constants of the continuity and boundary conditions. The frequencies and displacement mode shapes can be calculated as the eigenvalues (λ_i) and eigenvectors (C_i) of this equation set. Moreover, the strain mode shape can also be obtained by Eq. (19).

7. Analytical results and discussions

Figs. 7–11 illustrates the analytical results bringing out the influence of delamination size ($\bar{b}$), spanwise and thickness-wise locations ($\bar{a}_c$ and $\bar{d}_2$) of the delamination on the change of natural frequency and strain mode shape of the delaminated beam.

In Fig. 7, it shows the effect of the delamination size on the fundamental frequency of the central delaminated beam. Noticed that the frequency shift was calculated by (natural frequency of the intact beam − natural frequency of the delaminated beam)/natural frequency of the intact beam. The table indicates that the natural frequency would decrease due to the existence of the delamination. It is observed that the percentage of frequency shift is the highest while the delamination is located at the mid-plane ($\bar{d}_2=0.5$), and the frequency shift becomes smaller as the delamination location shifts towards the surface of the beam. The substantial effects of the delamination on the frequency shift are seen as the delamination size increases. However, for the delamination is only 10% or 20% of the

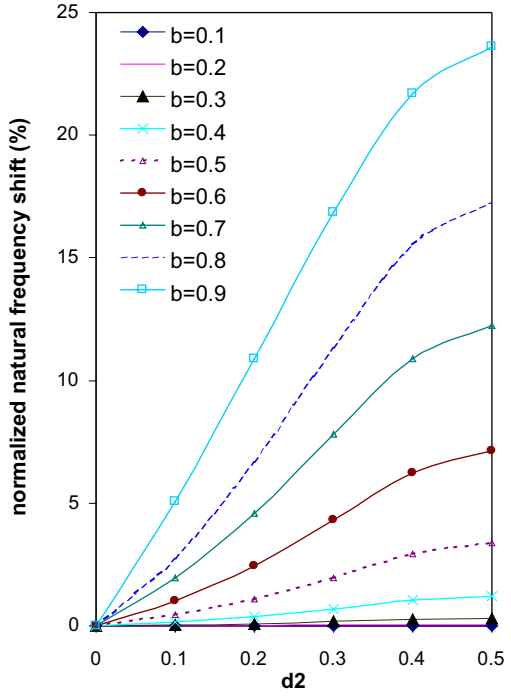

Fig. 7. Central delamination with different delamination sizes in mode 1.

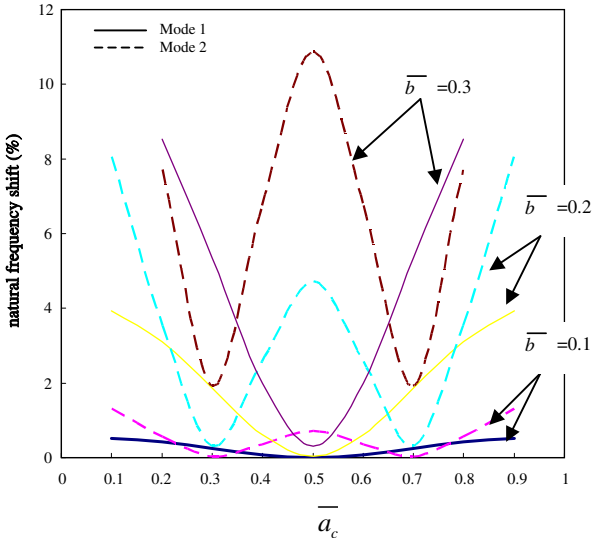

Fig. 8. Effect of spanwise location on the first and second natural frequencies with a 40% delamination.

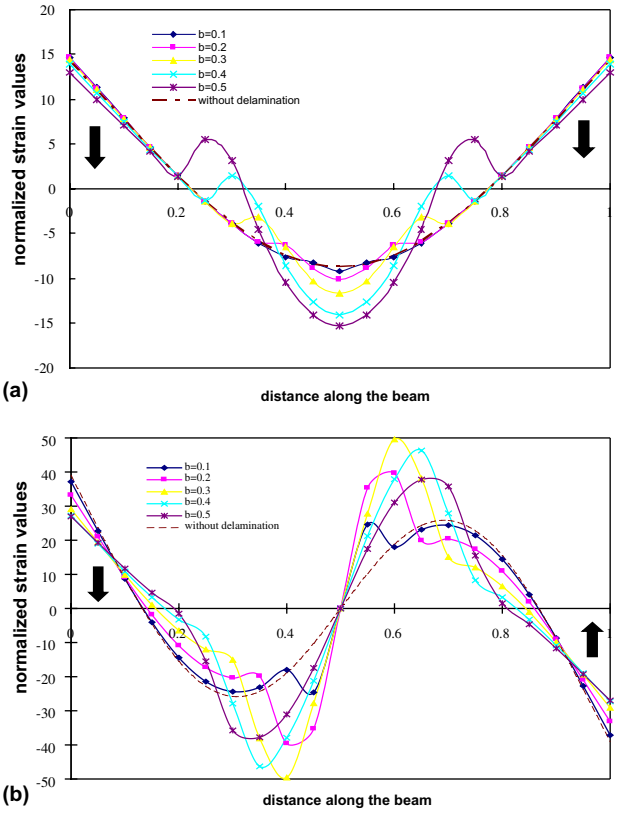

Fig. 9. (a) Strain mode shape with central delamination in middle layer with different sizes in mode 1; (b) strain mode shape with central delamination in middle layer with different sizes in mode 2.

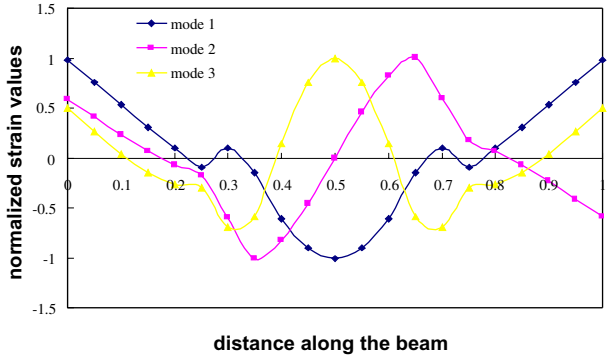

Fig. 10. Strain mode shape with 40% central delamination in middle layer with various modes.

total beam length, the changes of the fundamental frequency are not obvious, only approximately equal to 1%. It is reasonable to obtain those results as the delamination causes the reduction of the stiffness of the beam and hence leading the change of natural frequency.

Apart from the central delamination, Fig. 8 indicates the effect of spanwise location on the first and second natural frequencies with a 40% delamination for various delamination sizes respectively. The significant influence on the frequency shift due the delamination occurs in the different spanwise locations are noticed. The delamination effect on the natural frequency becomes minimum as $\bar{a}_c = 0.5$ at the first mode and $\bar{a}_c = 0.3$ and 0.7 at the second mode. Contrastively, that effect appears to be a maximum when the delamination located at the edges and central of the beam at modes 1 and

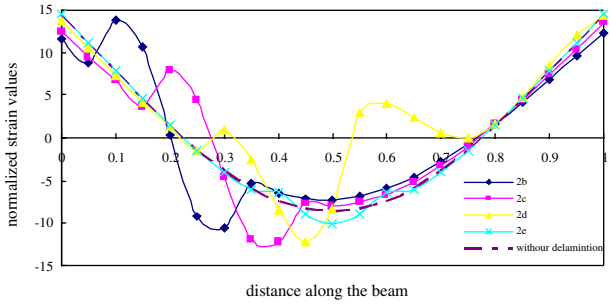

Fig. 11. Strain mode shape with 20% middle layer delamination in different spanwise locations.

2 respectively. As the delamination located at these locations, essential change of the natural frequency even for small delaminations ($\bar{b} = 0.1$ and 0.2) is observed. To explain this phenomenon, the displacement mode shapes of the clamped–clamped beam, as indicated in Fig. 5, and shear force which is proportional to the third derivative of the transverse displacement with respect to spanwise location are considered. As the weakening effect on natural frequency depends on the shear force, locating the delamination at the spanwise location with high shear force causes the large frequency shift. For a clamped–clamped beam, modes 1 and 3 are the symmetric modes. The curvature and shear force are the maximum and minimum at mid-span respectively. Therefore, the weakening effect on natural frequency is minimum for centrally located delamination ($\bar{a}_c = 0.5$) as shown in Fig. 8. Alternatively, for the asymmetric modes such as mode 2, it is seen that the curvature is zero and the shear force is maximum at mid-span. As the results, the weakening effect on natural frequency is a maximum when the delamination is located at centre of the beam as indicated in Fig. 8. It can be briefly concluded that the delamination effect on the natural frequency of the beam highly depends on the delamination size, vibrating mode, spanwise and thickness-wise locations.

Delamination not only affects the natural frequency, but also the strain mode shape of the beam. The effects of the delamination on the strain mode shapes of the beams are illustrated in Figs. 9–11. For the central delamination with various delamination sizes, the strain profile of the delaminated beams at the first mode is symmetric at the mid-span of the beam as shown in Fig. 9(a). Moreover, the changes of strains are observed at both edges of the delaminated beams in all cases, and it seems that the strain is seriously affected by increasing the delamination size. Compared with Fig. 9(a) and (b), the delamination effect on the strain mode shape of the beam is more obvious in mode 2. It is seen that the upward and downward shifts are observed at the ends of the beam with all delamination sizes. These upward and downward shifts indicate that the delamination effect is not restricted at the delaminated location, and it already affects the mechanical properties of a whole beam. To investigate the influence of the mode on the strain mode shape of the delaminated beam, Fig. 10 illustrates the strain mode shape with 40% central delamination in middle layer with different modes. It is known that the strain mode shape could be affected in the similar manner for the symmetric modes such as modes 1 and 3, but it is quite different for the asymmetric and symmetric modes, modes 1 and 2. As mentioned in the above, the influence of the delamination in the spanwise location on the natural frequency of the beam is not noticeable at the small delamination size. The effect of spanwise location on the fundamental frequency with small delamination, only 20% delamination size, in middle layer of the beam, was presented in Fig. 11. Significant changes of the strain due to the small delamination located at all spanwise locations are observed. Obvious disruption of the strain at the delamination area is noticed for the case 2e in which the delamination was centrally located. According to the above results on strain mode shape, it can be known that the delamination effect on the strain mode shape of the beam greatly depends on the delamination size, vibrating mode and spanwise location.

Based on the results of the delamination effect on the natural frequency and strain mode shape of the beam, it is summarised that the delamination influence of the strain mode shape is more obvious in all cases, especially for the small delamination, than that of the natural frequency. Additionally, in case of the various delamination sizes and locations, the same value of the frequency shift could be given in two different cases. The uniqueness of this value could not be guaranteed. Therefore, it is not accurate to use the change of the natural frequency for the aspect of delamination identification. However, if the strain mode shape is employed to combine with the natural frequency shift to be used for delamination detection, the reliability of the delamination identification results can be enhanced.

8. FBG sensor as a delamination detection device

Associated with the strain mode shape and the natural frequency shift of the delaminated beam, the delamination, even for the small one, could be effectively detected. Therefore, delamination location can be identified provided that the sensors can real-timely monitor the strain and natural frequency of the structures. In the above section, the FBG sensors were validated to be a dynamic strain monitoring device. In the following experimental study, the reliability of utilising the FBG sensors for natural frequency measurement of

intact and delaminated beams was also investigated. An experiment was performed in order to compare the measurements of the natural frequency of intact and delaminated beams by using an accelerometer, a laser vibrometer and a FBG sensor.

A clamped–clamped glass-fibre composite beam with embedment of a FBG sensor was fabricated. An accelerometer and the measurement point of the laser vibrometer was bonded and pointed to the surface of the beam at the same position where the FBG sensor was embedded respectively. Since the mass of the accelerometer could affect the accuracy of the natural frequency of the beam, the FBG sensor and the laser vibrometer were used to measure the natural frequency of the beam simultaneously without bonding the accelerometer on the beam surface. On the other hand, the natural frequency of the beam was measured by the accelerometer separately under the same experiment configuration as the one used for the FBG sensor and the laser vibrometer.

The frequency response function of the clamped–clamped intact beam was plotted in Fig. 12. It is clearly observed that a good agreement of the FBG sensor and the laser vibrometer is demonstrated. However, the mismatching of the accelerometer and laser vibrometer is indicated. This inconsistent result might be due additional mass of accelerometer that affects the natural frequency of the beam.

In order to investigate the natural frequency shift of the delaminated beam, delaminations were made by inserting Telfon film between 5th and 6th layer-laminates of the 10-layer glass-fibre composite beam to simulate the middle layer delamination as mentioned in the previous analytical model, as shown in Fig. 13. The experimental results are listed in Table 2. The FBG sensor and the laser vibrometer demonstrated the fact that the reduction of the natural frequencies of the beam due to the 25% delamination of the beam. As the results, the FBG sensor could detect the existence of the delamination by comparing the natural frequency of the delaminated beam and the intact one.

However, it is found that the natural frequencies measured by the accelerometer of the delaminated beam slightly increased at 1st and 3rd modes and decreased at the second mode in Table 2. The reason is that the mass effect of the accelerometer dominated the delamination effect on the natural frequencies at the 1st and 3rd modes, so that the natural frequencies of the delaminated beam increased. As the mode shape of mode 2 was different from that of the modes 1 and 3, the mass effect of the accelerometer might be ignorable. As the results, the delamination effect on the natural frequency was normally shown at second mode.

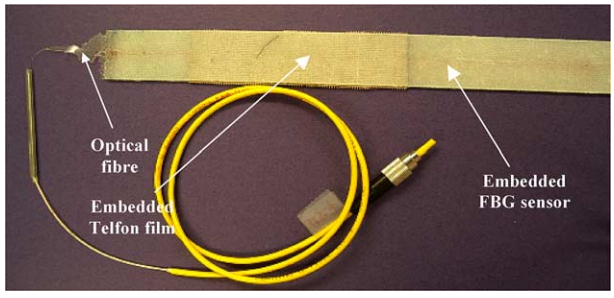

Fig. 13. Glass-fibre composite beam with 25% delamination simulated by inserting thin Telfon film.

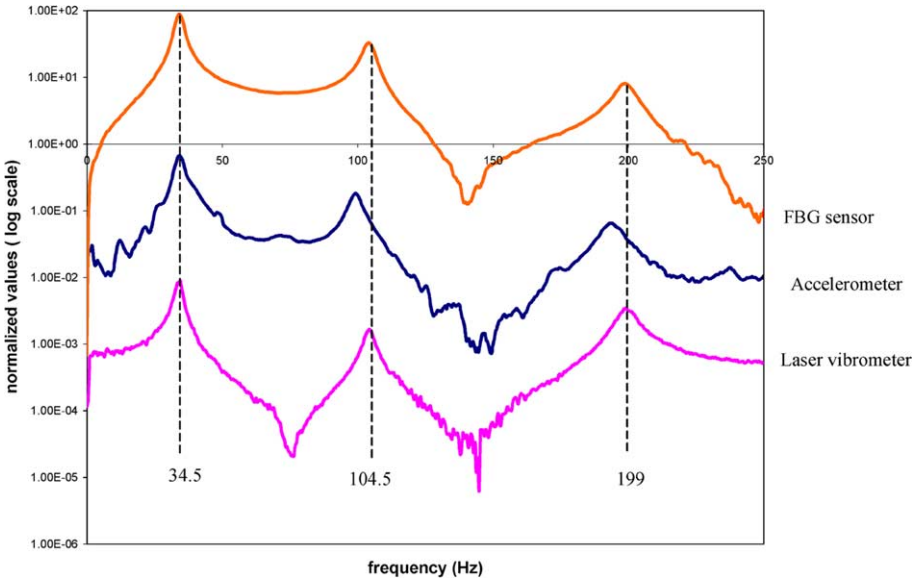

Fig. 12. The frequency response function of the clamped–clamped intact beam.

Table 2
The experimental results of natural frequencies of the beam without and with 25% delamination measured by an accelerometer, a laser vibrometer and a FBG sensor

Sensors	Natural frequency of beam without delamination (Hz)			Natural frequency of beam with 25% delamination (Hz)		
	Mode 1	Mode 2	Mode 3	Mode 1	Mode 2	Mode 3
Accelerometer	34.5	101.5	198.5	35.5	95	200
Laser vibrometer	34.5	104.5	199	34.5	93	196.5
FBG sensor	34.5	104.5	199	34.5	93	196.5

9. Conclusion

Dynamic strain measurement and delamination detection of clamped–clamped composite structures using embedded multiplexed FBG sensors through experimental and theoretical approaches are presented. It was revealed experimentally that the multiplexed embedded FBG sensors could measure the dynamic strain profile of an intact beam at certain natural frequency provided that the sensors are correctly mapped. Based on the theoretical results of a constrained model of a delaminated beam, the delamination effect on the natural frequency and strain mode shape of the beam highly depends on the delamination size, vibrating mode, spanwise and thickness-wise locations. Comparatively, the delamination effect is more observable on the strain mode shape than the natural frequency of the beam, especially for the beam with a small delamination. Therefore, combined with the results of the strain mode shape and the natural frequency shift of the delaminated beam, the delamination, even for the small one, could be effectively detected. Moreover, FBG sensors showed the comparable results with a laser vibrometer for measuring the natural frequency of the beam. The existence of delamination could be identified experimentally by unitising the FBG sensors. In the future work, it is valuable to develop an embedded multiplexed FBG sensor mapping system for delamination detection for advanced composite structures.

Acknowledgements

This project is partly supported by the Hong Kong Polytechnic University Grant and Research Grants Council of Hong Kong Special Administrative Region (RGC PolyU 5165/02E).

References

[1] Ferdinand P, Magne S, Marty VD, Rougeault S, Maurin L. Applications of fiber Bragg grating sensors in the composite industry. MRS Bull 2002;27(5):400–7.
[2] Lau KT, Zhou LM, Yuan LB, Woo CH. Strain monitoring in FRP laminates and concrete beam using FBG sensors. Compos Struct 2000;51:9–20.
[3] Davis MA, Kersey AD, Sirkis J, Friebele EJ. Shape and vibration mode sensing using a fibre optic Bragg grating array. Smart Mater Struct 1996;5:759–65.
[4] Read IJ, Foote PD. Sea and flight trials of optical fibre Bragg grating strain sensing systems. Smart Mater Struct 2001;10:1085–94.
[5] Kim CG, Lee JR, Tyu CY, Koo BY, Kang SG, Hong CS. In-flight health monitoring of a subscale wing using a fiber Bragg grating sensor system. Smart Mater Struct 2003;12:147–55.
[6] Zou Y, Tong L, Steven GP. Vibration-based model-dependent damage (delamination) identification and health monitoring for composite structures—a review. J Sound Vib 2000;230(2):357–78.
[7] Wang JTS, Liu YY, Gibby JA. Vibration of splite beams. J Sound Vib 1982;84:491–502.
[8] Mujumdar PM, Suryanarayan S. Flexural vibrations of beams with delaminations. J Sound Vib 1988;125:441–61.
[9] Lau KT. Fibre-optic sensors and smart composites for concrete applications: a review article. Mag Concr Res 2003;55(1):19–34.
[10] Maaskant R, Alavie T, Measures RM, Tadros G, Rizkalla SH, Guhathakurta A. Fibre-optic Bragg grating sensor for bridge monitoring. J Cem Concr Compos 1997;19:21–33.
[11] Saouma VE, Anderson DZ, Ostrander K, Lee B, Slowik V. Application of fibre Bragg grating in local and remote infrastructure health monitoring. J Mater Struct 1998;31:259–66.
[12] Clarence W. Vibration fundamentals and practice. CRC Press; 2000.